Optical Engineering

SPIEDigitalLibrary.org/oe

Optimization of rapid Mueller matrix imaging of turbid media using four photoelastic modulators without mechanically moving parts

Sanaz Alali
I. Alex Vitkin

SPIE

Optimization of rapid Mueller matrix imaging of turbid media using four photoelastic modulators without mechanically moving parts

Sanaz Alali
University of Toronto
Division of Biophysics and Bioimaging, Ontario Cancer Institute/University Health Network
Department of Medical Biophysics
610 University Avenue
Toronto, Ontario, M5G 2M9 Canada
E-mail: sanaz.alali@mail.utoronto.ca

I. Alex Vitkin
University of Toronto
Division of Biophysics and Bioimaging, Ontario Cancer Institute/University Health Network
Department of Medical Biophysics
610 University Avenue
Toronto, Ontario, M5G 2M9 Canada
and
University of Toronto
Department of Radiation Oncology
610 University Avenue
Toronto, Ontario, M5G 2M9 Canada

Abstract. A new method based on four photoelastic modulators (PEMs) and a charged couple device (CCD) camera, to rapidly image the samples' entire Mueller matrix, is proposed and optimized. The full imaging of Mueller matrix elements using time-gated technique synchronized with the four PEMs' modulation is demonstrated. Evolutionary algorithm is employed to choose the 16 time points, from which the Mueller matrix elements can be recovered with minimized sensitivity to noise. The suitability of several configurations of four PEMs with different frequencies and optical axes for the proposed imaging method is discussed through numerical examples. The ability to perform Mueller matrix imaging in the millisecond range with improved SNR in the absence of mechanically moving parts should prove advantageous in polarimetric characterization of biological tissues. [DOI: 10.1117/1.OE.52.10.103114]

Subject terms: polarimetric imaging; Mueller matrix; photoelastic modulator; tissue characterization.

Paper 130936 received Jun. 27, 2013; revised manuscript received Sep. 9, 2013; accepted for publication Sep. 10, 2013; published online Oct. 25, 2013.

1 Introduction

Mueller matrix analysis using polarized light is a powerful characterization technique with applications in thin film ellipsiometry, aerosol characterization, and biomedical diagnosis.[1–8] Imaging the Mueller matrix, as opposed to point detection, is highly desirable in biomedical applications, since most biological tissues are spatially heterogeneous.[7,8] The Mueller matrix should be measured in the shortest time to avoid *in vivo* motion artifacts. The fastest polarimetric imaging scheme is the so-called snapshot systems. These techniques diffract different polarizations of the light beam and extract the polarimetric information from filtering the frequency content of the final image, at the expense of some image information loss due to filtering.[9] The second category is the imaging systems that use switchable liquid crystals (LCs) to measure the sample's Mueller matrix in few seconds.[10–12] These systems can be optimized to decrease error sensitivity and are used for high-resolution imaging. Finally, the photoelastic modulator (PEM)-based systems are known to be the most sensitive due to the high and fast modulation of the PEMs, which enables synchronized detection.[13,14] The PEM aperture is large, which makes them ideal for imaging application. Moreover, the modulation efficiency of the PEMs is superior to polarization gratings and fast LCs.[15] Recently, Arteaga et al. have implemented four PEM polarimetric point detection scheme (originally suggested by Thompson et al.[16]), which can measure the full Mueller matrix of turbid media.[15,16] A corresponding system is now offered as a commercial product from Hinds Instruments, Hillsboro, Oregon.[17] Nevertheless, it is time consuming to construct images from a point detection system, since mechanical scanning of the sample or steering the beam followed by image stitching will be necessary.[15]

Here, we suggest a new method of recovering the Mueller matrix images using four PEMs and field-programmable gate array (FPGA)-assisted sequential time gating approach. The work further extends our recent theoretical formulation and experimental demonstration of the two PEM-based Stokes imaging technique.[18] Here, we demonstrate how our proposed method analytically recovers the Mueller matrix images in time domain, within millisecond time frame, without sacrificing the image quality. Also, this method does not set any assumption on the examined sample and is applicable to arbitrary turbid media and biological tissues.

2 Theory: the System's Matrix and Time-Gated Imaging to Calculate the Sample's Mueller Matrix

Let us denote the 16 elements of the turbid media's Mueller matrix by m_{ij} ($i, j = 1, \ldots, 4$); these vary spatially and are, thus, functions of (x, y) unless otherwise noted. For an arbitrary turbid media, all 16 elements can be nonzero and are generally independent of each other; therefore, at least 16 independent equations are needed for their detemination. A general four PEM-based polarized light imaging system is illustrated in Fig. 1, where the polarization state generator (PSG) enables different polarizations to impinge on the sample, and the polarization state analyzer (PSA) detects different polarization states of the light after interaction with the sample. As shown

0091-3286/2013/$25.00 © 2013 SPIE

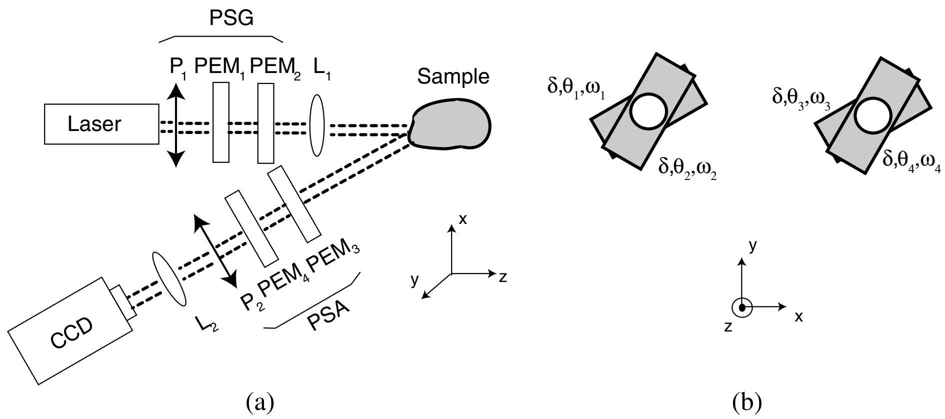

Fig. 1 (a) Mueller matrix imaging setup using two photoelastic modulators (PEMs) and a linear polarizer in both the polarization state generator (PSG) and the polarization state analyzer (PSA). (b) Each PEMi oscillates at a frequency f_i, and its optical axis is tilted at an angle θ_i. For simplicity, we set all PEM maximum retardances to be the same (δ_o common to all). P_1 and P_2 are polarizers, and L_1 and L_2 are lenses.

in Fig. 1, we use two PEMs and a linear polarizer in each of the PSG and the PSA.[15,16,19]

The polarization state of the light incident on the charged couple device (CCD) camera is described by a Stokes vector $\bar{S}_{\mathrm{out}}$, which is calculated from

$$\bar{S}_{\mathrm{out}}(t)=\begin{pmatrix} i(t)\\ q(t)\\ u(t)\\ v(t)\end{pmatrix} = M_{P2}M_{\mathrm{PEM4}}(t)M_{\mathrm{PEM3}}(t)\begin{pmatrix} m_{11} & m_{12} & m_{13} & m_{14}\\ m_{21} & m_{22} & m_{23} & m_{24}\\ m_{31} & m_{32} & m_{33} & m_{34}\\ m_{41} & m_{42} & m_{43} & m_{44}\end{pmatrix} \times M_{\mathrm{PEM2}}(t)M_{\mathrm{PEM1}}(t)\bar{S}_{\mathrm{in}}, \tag{1}$$

where i is the intensity, q, u, and v are the linear polarization (at 0 deg or 90 deg), linear polarization (at 45 deg or −45 deg), and the circular polarization, respectively. $M_{\mathrm{PEM}i}$ and M_{Pi} are the Mueller matrices of the i'th PEM and polarizer, respectively, and $\bar{S}_{\mathrm{in}}$ is the polarization state of the light issuing from the polarizer P_1 in the PSG. The overbars signify a 4-element vector, capital symbols represent 4×4 matrices, and the rest of the symbols represent numbers. The two PEMs and the polarizer in the PSG generate a time-varying Stokes vector $\bar{S}_g=[g_1(t)\quad g_2(t)\quad g_3(t)\quad g_4(t)]^T=M_{\mathrm{PEM1}}M_{\mathrm{PEM2}}\bar{S}_{\mathrm{in}}$. Similarly, the PEMs and the polarizer in the PSA detect a portion of light with the polarization that can be represented by a Stokes vector $\bar{S}_a(t)=[a_1(t)\quad a_2(t)\quad a_3(t)\quad a_4(t)]^T$, which is the transposition of the first row of the product of $M_{P2}\ M_{\mathrm{PEM3}}\ M_{\mathrm{PEM4}}$. As with any square-law detector, the CCD camera registers only the intensity of the light $i(t)$, the first element of $\bar{S}_{\mathrm{out}}$ in Eq. (1); when evaluated at time point t_k, this can be written as

$$i(t_k)=[a_1(t_k)\quad a_2(t_k)\quad a_3(t_k)\quad a_4(t_k)] \times\begin{pmatrix} m_{11} & m_{12} & m_{13} & m_{14}\\ m_{21} & m_{22} & m_{23} & m_{24}\\ m_{31} & m_{32} & m_{33} & m_{34}\\ m_{41} & m_{42} & m_{43} & m_{44}\end{pmatrix}\begin{pmatrix} g_1(t_k)\\ g_2(t_k)\\ g_3(t_k)\\ g_4(t_k)\end{pmatrix}, \tag{2}$$

where $i(t_k)$ stands for the integrated intensity on the CCD camera starting at time t_k (assuming a short-integration time as small as nanoseconds, which we will discuss later). As seen, $i(t_k)$ can be considered as a weighted sum of the sample's Mueller matrix elements modulated by the PSG and PSA functions as below

$$i(t_k)=\sum_{i=1}^{4}\sum_{j=1}^{4}(a_i g_j)m_{ij}, \tag{3}$$

or in terms of matrix algebra as

$$i(t_k)=\bar{Z}(t_k)\bar{M}, \tag{4}$$

with the 16 elements of the row vector $\bar{Z}(t_k)$ being

$$\begin{aligned}\bar{Z}(t_k)&=[z_1(t_k)\quad z_2(t_k)\quad \dots\quad z_{16}(t_k)]\\ &=[a_1(t_k)g_1(t_k)\ a_1(t_k)g_2(t_k)\ a_1(t_k)g_3(t_k)\ a_1(t_k)g_4(t_k)\dots\\ &\quad a_4(t_k)g_1(t_k)\ a_4(t_k)g_2(t_k)\ a_4(t_k)g_3(t_k)\ a_4(t_k)g_4(t_k)],\end{aligned} \tag{5}$$

and column vector $\bar{M}$ containing the 16 sample's Mueller matrix elements that we seek to determine

$$\begin{aligned}\bar{M}^T(t_k)=[&m_{11}\quad m_{12}\quad m_{13}\quad m_{14}\quad m_{21}\quad m_{22}\quad m_{23}\ \dots\\ &m_{24}\quad m_{31}\quad m_{32}\quad m_{33}\quad m_{34}\quad m_{41}\quad m_{42}\quad m_{43}\quad m_{44}].\end{aligned} \tag{6}$$

As mentioned, to find the 16 elements of vector $\bar{M}$ without ambiguity, 16 independent equations are needed. One way to do this is to acquire the intensity i at 16 time points t_k as follows:

$$\begin{bmatrix} i(t_1) \\ \vdots \\ i(t_{16}) \end{bmatrix} = Z\bar{M}, \tag{7}$$

where Z is a 16×16 element matrix composed of $\bar{Z}$ row vectors evaluated at 16 time points t_k

$$Z = \begin{pmatrix} \bar{Z}(t_1) \\ \bar{Z}(t_2) \\ \vdots \\ \bar{Z}(t_{15}) \\ \bar{Z}(t_{16}) \end{pmatrix}. \tag{8}$$

We call Z as the system matrix. If we choose $t_1, \ldots, t_{16}$ to yield a nonsingular system matrix Z, we can calculate the sought-after sample Mueller vector $\bar{M}$ from direct product of the inverse of matrix Z and the acquired intensities as

$$\bar{M} = Z^{-1} \begin{bmatrix} i(t_1) \\ \vdots \\ i(t_{16}) \end{bmatrix}. \tag{9}$$

To ensure a stable solution for $\bar{M}$ from Eq. (9), the determinant of matrix Z (which is a 16×16 square matrix) should be far from zero, to avoid singularity.[20] For $\bar{M}$ to be less sensitive to errors, usually, the condition number of Z should also be minimized.[19,20–23] Condition number is defined as $\kappa(Z) = \|Z\| \|(Z)^{-1}\|$ with $\| \|$ being the second-degree norm. The condition number sets an upper limit on the recovery error; basically, the error of recovering $\bar{M}$ will be less than $\kappa(Z)$ times the error of measuring the intensity $i(t)$. The time points $t_1, \ldots, t_{16}$ should be, then, chosen to yield a nonsingular system matrix Z with minimum condition number.

3 Evolutionary Algorithm for Optimizing the System's Matrix of Any PEMs Configuration

System matrix Z solely depends on the PSG and the PSA; in other words, $\bar{S}_g(t)$ and $\bar{S}_a(t)$ should be chosen carefully to result in a nonsingular Z matrix with minimum condition number. Each PEM in the incident and the detection arms introduces a time-varying retardance $\delta(t)$:

$$\delta_i(t) = \delta_o \sin(2\pi f_i t + \varphi_i), \tag{10}$$

where δ_o is the maximum modulation amplitude, f_i is the oscillation frequency, and ϕ_i is a phase. Most commercial PEMs are resonant devices with fixed modulation frequencies in the range of 20 to 100 kHz. Further, the modulation axis of each PEM can be differently oriented by tilting the device in the x-y plane. Hence, many different configurations of the system setup, as depicted in Fig. 1, are possible by selecting different values of fs and θs (the maximum retardance of each PEM, δ_o, was chosen to be the same for all four devices; this was partly for simplicity and partly because judicious selections of the four frequencies and orientation angles were sufficient to recover $\bar{M}$ as below). For each $(f_i, \theta_i)_{i=1-4}$ configuration, one should find the 16 time points that result in a well-posed matrix Z with minimum condition number.

This is a large-scale problem that has no analytical solution and cannot be optimized by blind search in a short time.[24] Such large-scale optimization problems can be tackled by heuristic approaches including genetic and evolutionary algorithms (EAs).[24] These terms stem from the similarity with biological concepts viz. parent and offspring iteration layers, gene on–off alterations in the binary representation of the parent/offspring mathematics, sexual-like (two-parents to yield an offspring, ∼mitosis) and asexual-like (single-parent to yield an offspring, ∼meiosis) paradigms, and so on. In recent years, these algorithms have been used to solve various problems in optics such as focusing light through turbid media, designing optical thin films, focusing fields with desired fluence profile, shaping femtosecond pulses, generating nondiffractive beams,[25–28] and even recently minimizing the condition number of LC and PEM-based polarimetric systems.[11,18] Here, we use the EA initially proposed by Massoumian et al.[25] Figure 2 is a simple schematic of how EA is applied to select the 16 time points that give the minimum condition number of the system matrix Z; also, minimum difference of t_i and t_{i-1} is dt and maximum difference of t_{16} and t_1 is T, which is the common period of the PEM oscillations. The algorithm starts with a randomly generated solution vector of $t_1, \ldots, t_{16}$. The solution vector randomly evolves by iterating via combinations of the two operators implemented in the algorithm: asexual parent–offspring mutation and sexual parent–offspring recombination.[25] The solution vector, which minimizes the condition number of Z in each iteration, survives and evolves during the next iterations. The iteration ends when the condition number of Z (the objective function) does not decrease after some reasonable computation time (∼3 min in our study).

4 Results and Discussion

By applying EA to a variety of configurations in Fig. 1, we found that there are many possible configurations with four PEMs that yield nonsingular matrix Z. To reduce the number of variables for the demonstration purposes, we chose the maximum retardance amplitude δ_o to be π for all the PEMs. The phases $\phi_i s$ were set to zero for these examples; although, more discussion about this is provided below. Also, we chose the frequencies f_i to be an integer, which are multiples of 10 kHz; this insures a periodic behavior for the imaging system, with a time period of 0.1 ms. Therefore, the input variable T was set to 0.1 ms; in other words, EA was set to look for the fittest $t_1, \ldots, t_{16}$ within

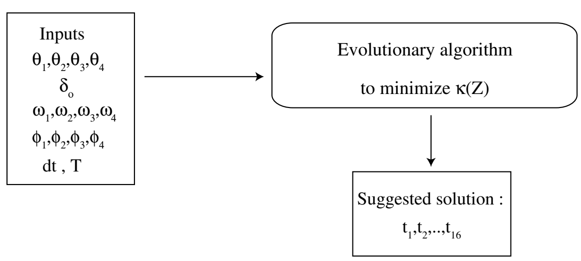

Fig. 2 Applying evolutionary algorithm (EA) to the polarimetry imaging system of Fig. 1 to find 16 time points from which the Mueller matrix image can be recovered via Eq. (9).

0.1 ms. For all the EA trials, the smallest time difference between the points $(t_i - t_{i-1})$ was set to $dt = 1\ \mu s$. Tables 1 and 2 present several preselected "reasonable" configurations and their resulting time points found by EA, which minimize $\kappa(Z)$.

As seen from Tables 1 and 2, several variations of the frequencies and optics axis orientations of the four PEMs are possible for successful recovery of the Mueller matrix images. The resultant $t_1, \ldots, t_{16}$ found by EA are unique for each setup and result in an invertible system matrix Z. However, the condition numbers are not close to 1, which means that the recovery procedure will be sensitive to noise. Finally, these results are specific to the selected horizontal orientations of the polarizers P_1 and P_2; if these change, new optimal $t_1, \ldots, t_{16}$ will be generated (results not shown).

This procedure is rigorous when the phases $\phi_i s$ are exactly known; whereas, in real life, the frequencies of the PEMs slightly drift, and $\phi_i s$ [in Eq. (10)], thus, randomly change in time.[15,18] One solution to this experimental problem is to find the times at which the PEMs are in certain phase differences relative to each other. We have recently demonstrated the practical feasibility of this method for a two PEMs-based Stokes imager.[18] We call our synchronization technique sequential time gating; briefly, an FPGA is used to sample the PEMs' reference frequencies, to detect the rising/falling edges, or to send a trigger to the CCD camera whenever the rising edges (falling edges) happens at the same time. By extending the same approach to four PEMs, the intensity of the modulated light can be acquired to resemble the periodic behavior of the PEMs, regardless of the frequency drifts. In other words, in sequential time gating, the PEMs' modulation follow Eq. (10) with fixed known phase ϕ_i.

To get some understanding of the experimental procedure and calibration, let us consider configuration V from Table 1 $[(f_i, \theta_i) = 30, 30; 40, 60; 50, 60; 20, 30]$ as an illustrative example. In real experimental settings, the PEMs' phases $\phi_i s$ randomly change. To acquire the 16 images at known fixed $\phi_i s$, FPGA-assisted sequential time gating should be used along with the calibration process.[18] To find the exact values of the phases through calibration: (1) several samples with known Mueller matrices, such as polarizers, are imaged; (2) the intensity $i(t)$) incident on the CCD camera, then, can also be simulated via Eq. (2) for each sample and for different ranges of $\phi_i s$; and (3) Then, the real values of fixed $\phi_i s$ can be found when the highest correlation between the experimentally acquired and simulated intensities occur.[18] Once the correct phases are found, the times in Table 2 have to be recalculated. Here, without the loss of generality, and for demonstration purposes, we simulated the intensity for configuration V when all the PEMs are in phase ($\phi_i = 0$), keeping in mind that different $\phi_i s$ will result in different waveforms for intensity $i(t)$ that can be easily simulated. The simulated incident intensity on the CCD camera with no sample (air) and when the sample is a linear polarizer at 0 deg are presented in Figs. 3(a) and 3(b), respectively. As shown, different samples result in different intensity variation forms, as described in Ref. 18. Moreover, the periodicity in intensity $i(t)$ [values being the same for t and $t + T$ in Figs. 3(a) and 3(b)] implies that experimental averaging is possible, which confers a significant SNR boost to the Mueller matrix imaging approach while still enabling rapid measurements. The total time in which a complete Mueller matrix can be extracted depends on the CCD frame rate. For example, a top-end CCD (e.g., PIMAX-3, Princeton Instruments, Trenton, New Jersey) can be set to acquire images with nanosecond gating time and has a data storage rate of about 50 frames per second. This means that the 16 intensity images can be captured and saved in milliseconds time. Since this time is relatively short, the 16 images at $t_1, \ldots, t_{16}$ [Eq. (9)] can be captured and averaged several times to boost up the SNR (by minimizing the effects of the random noise).

Next, we investigate on how acquiring the intensity at the EA-optimized 16 time points enables the extraction of the sample's Mueller matrix image. In Fig. 4, we have simulated the performance of configuration V and its Mueller matrix recovery capability using the 16 time points optimized through EA (Table 2). To test the full ability of the Mueller matrix imaging procedure, we chose a complicated Mueller matrix, as illustrated in Fig. 4(a), from a heterogeneous bilayered turbid medium modeled by PolMC code, as described fully in Ref. 29. The phantom

Table 1 Examples of photoelastic modulator (PEM) configurations in Fig. 1 (with $P_1 = 0$ deg and $P_2 = 0$ deg) that can be used to fully recover the sample's Mueller matrix.

Configuration	f_1	θ_1	f_2	θ_2	f_3	θ_3	f_4	θ_4
I	30	60	40	90	50	90	20	60
II	30	60	20	90	50	90	20	60
III	30	45	60	90	50	90	20	45
IV	30	45	60	90	50	60	20	30
V	30	30	40	60	50	60	20	30

Note: The values of $f_i s$ are in kHz, and the values of $\theta_i s$ are in deg.

Table 2 The recovery times suggested by evolutionary algorithm (EA) for each configuration from Table 1, and the resultant condition number of the system matrix Z.

Configuration	$t_1, \ldots, t_{16}$ (μs)	$\kappa(Z)$
I	12, 17, 22, 28, 33, 37, 39, 42, 51, 63, 69, 73, 76, 80, 90, 93	6.7
II	5, 14, 21, 26, 31, 33, 41, 43, 49, 54, 66, 69, 70, 72, 94, 100	8.2
III	4, 9, 19, 21, 28, 33, 37, 59, 70, 72, 78, 80, 83, 88, 90, 92	13.3
IV	1, 2, 3, 20, 22, 27, 29, 36, 46, 49, 53, 55, 64, 68, 80, 82	13.8
V	1, 2, 3, 9, 15, 20, 26, 29, 33, 49, 54, 70, 73, 82, 99, 100	8.4

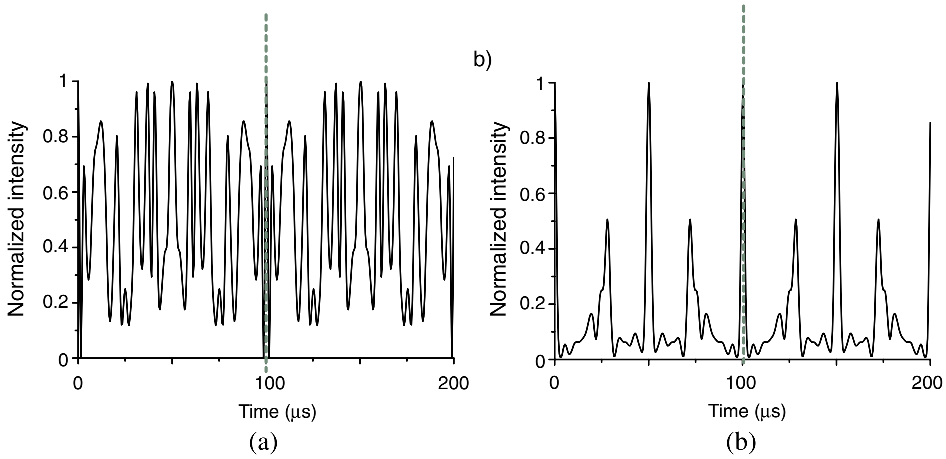

Fig. 3 Simulated intensity after the PSA [at the charged couple device (CCD)] for the configuration V of Table 1 over 200 μs, when (a) there is no sample and (b) the sample is a linear polarizer oriented at 0 deg. Dotted line at 100 ms shows the system period.

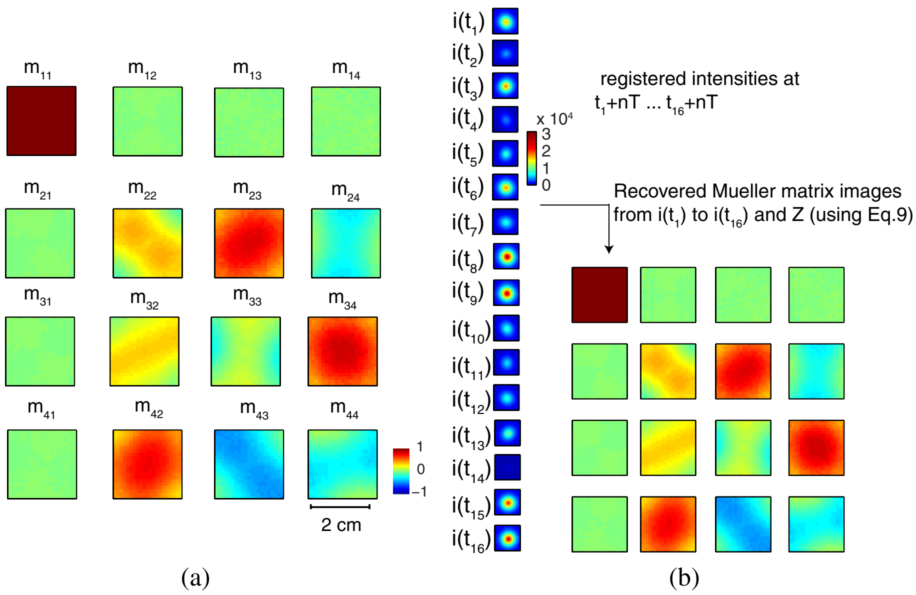

Fig. 4 (a) The input images of the examined sample Mueller matrix, stemming from a complex hereogenous turbid birefringent sample, produced by Monte Carlo simulation described in Ref. 29. (b) Recovering the Mueller matrix images using four PEM scheme of configuration V and the intensities registered at the EA selected times from Table 2.

was a $5 \times 5 \times 2\ \mathrm{cm}^3$ box with a scattering coefficient of $6\ \mathrm{cm}^{-1}$ and minimal absorption (equal to water's absorption at 635 nm). Birefringence magnitudes in layers 1 and 2 were equal to 0.000115, and the extraordinary axes orientation differed by 30 deg in the two layers. Figure 4(b) shows the PolMC simulations of the CCD signal $i(t_k)$ from Eq. (2) at times suggested by Table 2 and the recovered Mueller matrix using the inverse of Z via Eq. (9). As seen, the images of the Mueller matrix elements were fully recovered with $\sim$0 error (considering four precision digits), which implies that the analytical formulation and EA optimization are self-consistent and yield a correct solution in ideal conditions without noise.

Although we demonstrate $\sim$100% recovery in ideal conditions, the rather high condition numbers in Table 2 imply high sensitivity to noise. To investigate this further, 5% random noise was added to the registered intensities $i(t_1), \ldots, i(t_{16})$ which resulted in the recovered Mueller images, as demonstrated in Fig. 5. The fractional error of recovering Mueller matrix elements [except the elements with values close to 0 (first row and column)] is illustrated in Fig. 5(b). As seen in the bar graph, the mean value of error is less than 5%, and the maximum standard deviation is 12%. One way to reduce this sensitivity is to acquire more images in each period (increase the number of the time points to more than 16) and make the Z matrix an over-determinant matrix. The condition number of such a matrix can be optimized to be closer to 1 and will result in less sensitivity to noise. This procedure will be explored in a future experimental publication.

Finally, one should note that there are some $(f_i, \theta_i)_{i=1-4}$ configurations which will not work in our scheme, i.e., they cannot generate a nonsingular Z matrix. In such cases, EA

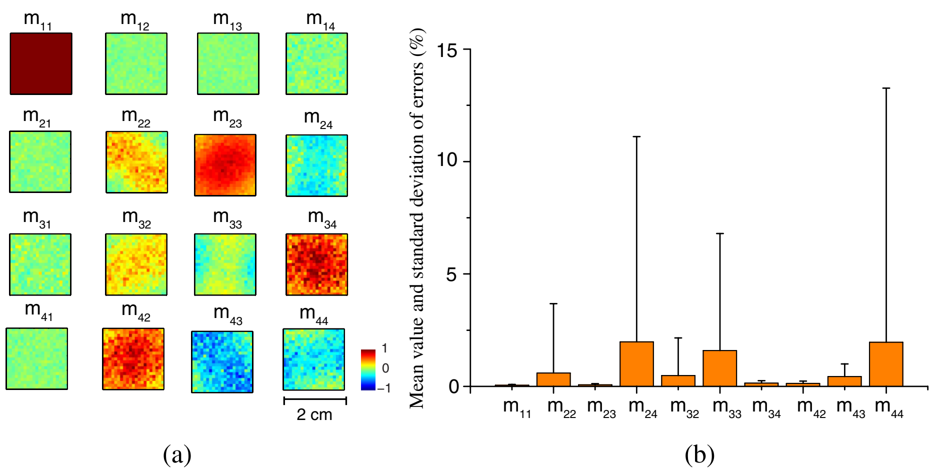

Fig. 5 (a) Recovered Mueller matrix images of Fig. 4(a) when 5% random noise was added to the measured intensities. (b) The bars show the mean value of the recovery error in each element over the entire image in (a), while the error bars indicate the standard deviation of the recovery error.

Table 3 Examples of PEM configurations that cannot be used to recover Mueller matrix images with the suggested methodology.

Configuration	f_1	θ_1	f_2	θ_2	f_3	θ_3	f_4	θ_4
A	30	60	40	90	50	45	20	0
B	30	60	40	90	50	90	20	0
C	30	45	40	45	50	90	20	60
D	30	60	40	90	30	90	20	60
E	20	60	50	90	50	90	20	60
F	20	60	30	90	50	90	20	60

Note: The values of f are in kHz, and the values of θ are in deg.

fails to find independent vectors $\bar{Z}(t_1), \ldots, \bar{Z}(t_{16})$. A few examples of such configurations are listed in Table 3.

The first category (cases A–C) are those whose PSG and/or PSA do not generate enough different Stokes vectors, due to the particular optic axis orientation θ_i of the PEMs with respect to each other and the polarizers P_1 and P_2. To demonstrate the inadequate performance of these failed configurations, we present the corresponding Poincare sphere representations[30] of the poor θ_i states (A–C) in Fig. 6. As seen in Figs. 6(a) and 6(b), the Stokes vectors $\bar{S}_g$ or $\bar{S}_a$ sample limited regions of the Poncaire sphere, compared with a "good" arrangement (configuration I, Table 1) of Fig. 6(c), where both $\bar{S}_g$ and $\bar{S}_a$ cover nearly the whole sphere surface.

The second category (cases D–F) contains the PSG and the PSA configurations that are highly correlated in time through inappropriate selections of the four PEM modulation frequencies. In such cases, the polarization states of PSG and PSA change together due to their frequency combinations, which result in insufficient temporal separation of the 16

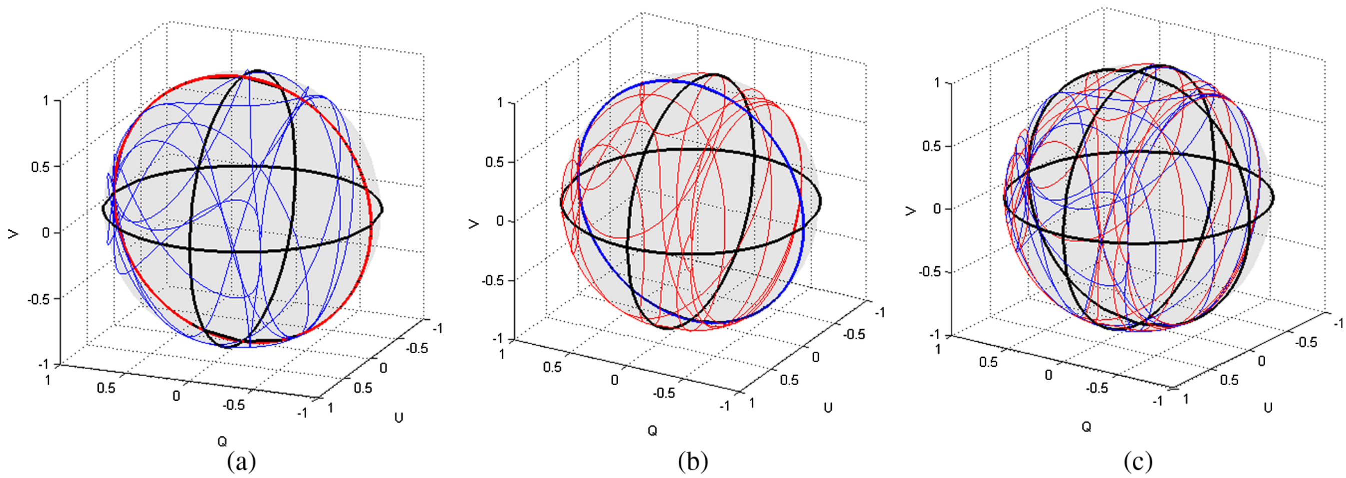

Fig. 6 Temporal polarization trajectories of polarization states for different experimental configurations generated by PSA (red) and PSG (blue) states represented on the Poincare sphere. Shown in black are the reference circles on the Poincare sphere (equator and two of the meridians for better three-dimensional illustration). Poor θ arrangements (Table 3) are shown in (a) configuration A and (b) configuration C, which demonstrate inadequate polarization state coverage. (c) A useful arrangement from Table 1 (configuration I) is shown.

Table 4 Correlation between polarization states of selected polarization state generator (PSG) and polarization state analyzer (PSA) elements in different configurations, as quantified by the correlation coefficient r.

Configuration	$r[a_2(t), g_2(t)]$	$r[a_3(t), g_3(t)]$	$r[a_4(t), g_4(t)]$
I	0.0085	0.1381	−0.2064
E	1	1	−1
II	0.0085	0.0358	−0.1670
F	1	−0.1707	−0.1597

Note: I and II are useful configurations from Table 1, and E and F are examples of poor configurations from Table 3.

requisite time points. In Table 4, the highly correlated nature of $\bar{S}_g$ and $\bar{S}_a$ in E–F configurations is contrasted to minimal correlation of configurations I and II from Table 1 (that do successfully recover the Mueller matrix images).

5 Conclusion

In conclusion, we proposed a camera-based Mueller matrix imaging technique using four PEMs applicable to arbitrary samples including complex heterogeneous turbid media such as biological tissues. Unlike prior point-measurement systems that use synchronous detection to lock in on the four frequencies and their harmonics, we meet the challenge of imaging-based high SNR detection via temporal gating algorithm implementable on a CCD-based Mueller matrix polarimeter. Specifically, a practical approach based on an EA was developed to select the 16 optimal time points at which the camera-detected intensities should be recorded, and, then, analyzed with matrix algebra to yield the sample Mueller matrix. The challenges of overcoming PEMs frequency drift were also foreseen and handled using previous experimentally demonstrated method with FPGA. The overall methodology was demonstrated for Mueller matrix inversion recovery using simulated turbid medium imaging data in ideal conditions and in the presence of noise. Four different PEM configurations with varying modulation axis orientations and modulation frequencies were examined and interpreted, in terms of their suitability for this method. As no filtering was needed in this approach, the spatial resolution and the contrast of the recovered Mueller matrix images were not compromised. Overall, the ability to rapidly and robustly obtain Mueller matrix images with PEM-based polarization modulation approach should prove advantageous in the rapidly expanding field of turbid Mueller matrix imaging polarimetry.

References

1. G. Jin, R. Jansson, and H. Arwin, "Imaging ellipsometry revisited: developments for visualization of thin transparent layers on silicon substrates," *Rev. Sci. Instrum.* **67**(8), 2930–2936 (1996).
2. Y. M. Bae et al., "Immunosensor for detection of Yersinia enterocolitica based on imaging ellipsometry," *Anal. Chem.* **76**(6), 1799–1803 (2004).
3. Y. J. Kaufman, D. Tanre, and O. Boucher, "A satellite view of aerosols in the climate system," *Nature* **419**(6903), 215–223 (2002).
4. S. L. Jacques, J. R. Roman, and K. Lee, "Imaging superficial tissues with polarized light," *Lasers Surg. Med.* **26**(2), 119–129 (2000).
5. R. S. Gurjar et al., "Imaging human epithelial properties with polarized light-scattering spectroscopy," *Nat. Med.* **7**(11), 1245–1248 (2001).
6. M. F. G. Wood, D. Cote, and I. A. Vitkin, "Combined optical intensity and polarization methodology for concentration determination in simulated optically clear and turbid biological media," *J. Biomed. Opt.* **13**(4), 044037 (2008).
7. S. Alali et al., "Optical assessment of tissue anisotropy in ex vivo distended rat bladders," *J. Biomed. Opt.* **17**(8), 109801 (2012).
8. A. Pierangelo et al., "Polarimetric imaging of uterine cervix: a case study," *Opt. Express* **21**(12), 14120–14130 (2013).
9. M. W. Kudenov et al., "Snapshot imaging Mueller matrix polarimeter using polarization gratings," *Opt. Lett.* **37**, 1367–1369 (2012).
10. A. Pierangelo et al., "Multispectral Mueller polarimetric imaging detecting residual cancer and cancer regression after neoadjuvant treatment for colorectal carcinomas," *J. Biomed. Opt.* **18**(4), 046014 (2013).
11. P. A. Letnes et al., "Fast and optimal broad-band Stokes/Mueller polarimeter design by the use of a genetic algorithm," *Opt. Express* **18**(22), 23095–23103 (2010).
12. E. Garcia-Caurel, A. De Martino, and B. Drévillon, "Spectroscopic Mueller polarimeter based on liquid crystal devices," *Thin Solid Films* **455–456**, 120–123 (2004).
13. D. J. Diner et al., "First results from a dual photoelastic-modulator-based polarimetric camera," *Appl. Opt.* **49**(15), 2929–2946 (2010).
14. C. Y. Han and Y. F. Chao, "Photoelastic modulated imaging ellipsometry by stroboscopic illumination technique," *Rev. Sci. Instrum.* **77**(2), 023107 (2006).
15. O. Arteaga et al., "Mueller matrix polarimetry with four photoelastic modulators: theory and calibration," *Appl. Opt.* **51**(28), 6805–6817 (2012).
16. R. C. Thompson, J. R. Bottiger, and E. S. Fry, "Measurement of polarized light interactions via the Mueller matrix," *Appl. Opt.* **19**(8), 1323–1332 (1980).
17. http://www.hindsinstruments.com/products/polarimeters/mueller-polarimeter/.
18. S. Alali, T. Yang, and I. A. Vitkin, "Rapid time-gated polarimetric Stokes imaging using photoelastic modulators," *Opt. Lett.* **38**(16), 2997–3000 (2013).
19. J. S. Tyo, "Design of optimal polarimeters: maximization of signal-to-noise ratio and minimization of systematic error," *Appl. Opt.* **41**(4), 619–630 (2002).
20. S. Watkins, *Fundamentals of Matrix Computations*, John Wiley and Sons Inc., New York (1991).
21. A. Ambirajan and J. D. C. Look, "Optimum angles for a polarimeter: part I," *Opt. Eng.* **34**(6), 1651–1655 (1995).
22. D. Layden, M. F. G. Wood, and I. A. Vitkin, "Optimum selection of input polarization states in determining the sample Mueller matrix: a dual photoelastic polarimeter approach," *Opt. Express* **20**(18), 20466–20481 (2012).
23. K. M. Twietmeyer and R. A. Chipman, "Optimization of Mueller matrix polarimeters in the presence of error sources," *Opt. Express* **16**(15), 11589–11603 (2008).
24. C. H. Papadimitriou, *Computational Complexity*, Addison Wesley, Boston (1994).
25. F. Massoumian, S. Alali, and T. Mansouri, "Evolutionary algorithm for solving the inverse problem of finding the incident field on a high-aperture lens for generating a desired focused field," *Opt. Lett.* **34**(1), 67–69 (2009).
26. T. Baumert et al., "Femtosecond pulse shaping by an evolutionary algorithm with feedback," *Appl. Phys. B* **65**(6), 779–782 (1997).
27. A. Sanchez-Serrano et al., "Engineering of nondiffracting beams with genetic algorithms," *Opt. Lett.* **37**(24), 5040–5042 (2012).
28. N. Yamada and T. Nishikawa, "Evolutionary algorithm for optimization of nonimaging Fresnel lens geometry," *Opt. Express* **18**(S2), A126–A132 (2010).
29. S. Alali, Y. Wang, and I. A. Vitkin, "Detecting axial heterogeneity of birefringence in layered turbid media using polarized light imaging," *Biomed. Opt. Express* **3**(12), 3250–3263 (2012).
30. D. H. Goldstein, *Polarized Light*, Marcel Dekker, New York (2003).

Sanaz Alali has an MS degree in optics and microwaves from Sharif University of Technology, Tehran, Iran, in 2006. She is currently pursuing her PhD in biophotonics (medical biophysics) at the University of Toronto, Toronto, Canada. Her research area focuses on studying polarized light interaction with biological tissues, including Mueller matrix analysis and developing new methods of measuring Mueller matrix.

I. Alex Vitkin is an engineering physicist/biomedical engineer by training, with further specialization in medical physics and biomedical optics. He is currently a professor of medical biophysics and radiation oncology at the University of Toronto, a senior scientist at the Ontario Cancer Institute, and a clinical medical physicist at Princess Margaret Hospital (all in Toronto, Ontario, Canada). He has published over 140 papers and book chapters on diagnostic and therapeutic uses of light in biomedicine, consults for biophotonics companies, and currently serves as a topical editor of *Optics Letters*. He has lectured widely at national and international levels, including delivering special seminars and summer school modules on biophotonics in Mexico, Brazil, Taiwan, New Zealand, Ukraine, Germany, Cyprus, and Russia; he is currently an active participant in the SPIE Visiting Lecturer and OSA Travelling Lecturer programs. He is also a board-certified medical physicist, and a fellow of OSA and SPIE.